

Date of publication xxxx 00, 0000, date of current version xxxx 00, 0000.

Digital Object Identifier 10.1109/ACCESS.2017.Doi Number

An Adaptive Hybrid Beamforming Approach for 5G-MIMO mmWave Wireless Cellular Networks

Spyros Lavdas¹, Panagiotis Gkonis², Zinon Zinonos¹, Panagiotis Trakadas² and Lambros Sarakis²

¹Department of Computer Science, Neapolis University, Paphos, 8042, Cyprus. E-mails: {s.lavdas, zinon.zinonos}@nup.ac.cy

²General Department, National and Kapodistrian University of Athens, Sterea Ellada, 34400 Dirfies Messapies, Greece.

E-mails: {pgkonis, ptrakadas,lsarakis}@uoa.gr

Corresponding author: Spyros Lavdas (s.lavdas@nup.ac.cy).

“This work has been partially supported by the Affordable5G project, funded by the European Commission under Grant Agreement H2020-ICT-2020-1, number 957317 through the Horizon 2020 and 5G-PPP programs (www.affordable5g.eu).”

ABSTRACT Hardware complexity reduction is a key concept towards the design and implementation of next generation broadband wireless networks. To this end, the goal of the study presented in this paper is to evaluate the performance of an adaptive hybrid analog-digital beamforming approach in fifth-generation (5G) massive multiple input multiple output (MIMO) millimeter wave (mmWave) wireless cellular orientations. In this context, generated beams are formed dynamically according to traffic demands, via an on-off analog activation of radiating elements per vertical antenna array, in order to serve active users requesting high data rate services without requiring any expensive and mechanical complex steering antenna system. Each vertical array, which constitutes a radiating element of a circular array configuration, has a dedicated radio frequency chain (digital part). The performance of our proposed approach is evaluated statistically, by executing a sufficient number of independent Monte Carlo simulations per MIMO configuration, via a developed system-level simulator incorporating the latest 5G-3GPP channel model. According to the presented results, the adaptive beamforming approach can improve various key performance indicators (KPIs) of the wireless orientation, such as total downlink transmission power and blocking probability. In particular, when studying/analyzing a MIMO configuration with 15 vertical antenna arrays and 10 radiating elements per array, then, depending on the tolerable amount of transmission overhead, the proposed adaptive algorithm can significantly reduce the number of active radiating antenna elements compared to the static grid of beams case. In the same context, when keeping the number of radiating elements constant, then the total downlink transmission power as well as the blocking probability can be significantly reduced. It is important to note that all the KPIs have been extracted when deploying the developed array configuration in complex cellular orientations (two tiers of cells around the central cell).

INDEX TERMS 5G, hybrid beamforming, massive MIMO, millimeter wave communications, system-level simulations

I. INTRODUCTION

As the deployment of fifth-generation (5G) broadband wireless cellular networks is becoming a reality, the provision of zero latency high data rate services to mobile users is inextricably connected with a holistic network redesign [1]. In this context, various novel technologies have been introduced in order to support the 5G vision: millimeter wave (mmWave) transmission [2]-[3], non-orthogonal multiple access (NOMA) [4]-[5] as well as massive multiple input multiple output (MIMO) architectures [6]-[7]. In the latter case, a large number of antenna arrays is deployed at

the base stations (BSs) of a cellular orientation in order to support mobile stations (MSs) requesting high data rate services. This is achieved by the generation of highly directional beams that minimize multiple access interference (MAI).

In addition to 5G networks, the new forthcoming era of sixth-generation (6G) technology promises to connect everyone and everything, everywhere [8]. To this end, the necessary 5G equipment should be adapted to high frequency devices for multi-gigabit-per-second data speed applications (i.e., 20 Gbps for downlink and 10 Gbps for

uplink with latencies in the order of 1ms [9]) to be supported. Such type of bandwidth-hungry applications will need to be served by ultra-small communication devices [10]. Hence, the experience of the novel design and efficient operation of mmWave antenna configurations in 5G communication technology will shed light on the next day of 6G communications. It should be noted at this point that the deployment of mmWave antennas in a cellular system can lead to the design of powerful BSs in terms of flexible geometry and construction cost. Besides, the small size of mmWave antenna configurations provides the unique opportunity to have a multitude of flexible BS deployments for the support of mutable traffic and overall throughput improvement.

In traditional multi-user (MU) MIMO systems, fully digital (FD) precoding is the typical approach to adjust the amplitudes and phases of the transmitted signals in order to achieve optimum beamforming. However, in a massive MIMO configuration, FD approach would result in a significant computational and hardware burden, since the number of radio frequency (RF) chains is equal to the number of antennas. In this context, the majority of related works in literature focus on suboptimum beamforming algorithms, that are based on the hybrid beamforming (HBF) approach: the hybrid precoding architecture concatenates the digital precoder at baseband and the analog precoder in the RF domain. Therefore, benefiting from the low-dimensional digital precoder, fewer RF chains are required for implementation. In this paper, the performance of a low-complexity HBF structure is evaluated, when deployed in massive MIMO mmWave multicellular orientations.

A. RELATED WORK

In [11], a comprehensive survey is provided on hybrid multiple-antenna transceivers: hardware structures are distinguished based on their complexity, while Channel State Information (CSI) requirements are analyzed as well. In the same framework, in [12] several proposals of HBF structures in mmWave systems have been presented, focusing on three key aspects: hardware, spectral and computational efficiency. According to the presented analysis, with a suitable structure HBF can approach the performance of the FD one with low hardware complexity. In the same context, the authors demonstrate that it is sufficient to have a number of RF chains that is comparable to the number of the transmitted data streams and a small number of fixed phased shifters per transmitting antenna. In [13], a framework for hybrid precoder and combiner design has been presented, applicable to various channel models and hardware settings. This framework can be directly applied in massive MIMO systems deployed in 5G cellular orientations.

In an effort to further reduce hardware and algorithmic complexity, in [14] a new analog beamforming architecture is proposed, which only uses simple analog switches to achieve beamforming gains. According to the proposed

approach, both the full diversity gain and the full array gain can be achieved. However, results are limited to the case of one data stream for a point-to-point transmission. In [15], the authors have proposed a discrete Fourier transform (DFT)-assisted user clustering hybrid precoding algorithm for a hybrid analog-digital precoding-combining transceiver in mmWave MIMO systems. To this end, two possible structures for a hybrid architecture are defined, namely fully connected (FC) and partially connected (PC). In the first case, all the RF chains are connected to each antenna element, while in the second case only specific subsets of transmit antennas are connected to each one of the RF chains. According to the presented results, the FC structure has improved energy efficiency when only a few RF chains are employed; otherwise, the PC structure is preferable. In [16], a low-complexity power efficient transmitter is presented, that is based on a double layer structure combining information and azimuthal spatial directivity. According to the presented results, the proposed transmitter can achieve similar performance as conventional beamforming transmitters. In [17], it is shown that hybrid analog-digital beamforming can approach the performance of FD beamforming while requiring lower complexity. In [18], a HBF approach is presented that utilizes machine learning techniques to improve the achievable spectral efficiency (SE). To this end, the proposed two-step algorithm can attain almost the same efficiency as the one that can be achieved by FD architectures.

Other studies consider a specific HBF approach and focus on the optimization of the MU beamforming. In this context, in [19] an HBF design for orthogonal frequency-division multiplexing (OFDM)-based systems with large-scale antenna arrays is considered. According to the presented results, as also shown in [12], the FC architecture can approach the performance of the FD beamforming with a reasonable number of RF chains. In [20], considering a PC scheme, a deep neural network-based hybrid beamforming for the MU mmWave massive MIMO system is presented. This system is formulated as an autoencoder neural network, which is trained in a style of end-to-end self-supervised learning. According to the simulation results, considering a single-cell scenario, the proposed approach outperforms about 2 dB in terms of bit error rate (BER) performance compared with existing methods. In [21], the authors propose a low-feedback overhead hybrid analog-digital precoder and equalizer schemes for the uplink of massive MIMO mmWave heterogeneous networks systems. The results showed that the performance of the proposed schemes is quite close to the FD counterpart. In [22], a single cell downlink MU massive MIMO system working in a generic channel model with a hybrid structure that supports multiple streams per MS is considered. To this end, the proposed approach jointly designs the analog and digital stage by trying to avoid the loss of information at each stage. The derived solution has the fewest RF chains and is shown to

outperform the state of the art for HBF systems, even when the number of BS antennas is not very large. In [23], an HBF approach is introduced with dynamic subarrays and low-resolution phase shifters for a mmWave downlink MU system. In an effort to further reduce beamforming complexity, a simple heuristic hybrid beamformer design algorithm is presented as well. An extension of the aforementioned work for MU MIMO-OFDM systems is presented in [24]. In this context, the proposed hybrid beamformer algorithm aims at SE maximization and mean square error minimization. In [25], a MU MIMO downlink system is considered, where a two-stage HBF design approach tackling both SE and energy efficiency (EE) maximization is examined. To this end, in the first stage the analog beamforming parts are updated, which are then taken into account in the second stage to design the digital beamforming parts to maximize the system's EE or SE. Moreover, hardware constraints and realistic circuitry power consumption are taken into consideration as well. According to the presented results, the PC scheme achieves lower SE and EE compared to the FD approach for certain multiuser scenarios.

Interference mitigation is also taken into consideration towards the design of efficient low complexity HBF approaches. In [26], a hybrid MU framework is presented, for dynamic subarray formulation in massive MIMO systems. Simulation results show that the sum rate and the EE achieved by the dynamic subarray architecture significantly outperform those of the fixed subarray architectures. In [27], a hybrid MU equalizer for the uplink of broadband mmWave massive MIMO single carrier frequency-division multiple access (SC-FDMA) systems with dynamic subarray antennas was proposed and evaluated. Results indicate that the proposed approach can mitigate MU interference, achieving a BER performance quite similar to the one of the FC approach. In [28], an interference-aware pre-beamformer (analog beamformer) design for joint spatial division and multiplexing is presented, which is a user-grouping based two-stage beamforming method. To this end, single-carrier frequency domain equalization (SC-FDE) is employed in uplink frequency-selective channels. According to the presented results, most of the interference is suppressed with the help of the proposed constrained beamformers. In the same context, an iterative block decision feedback equalization (IB-DFE) method based on minimum mean square error criterion is proposed for the digital beamforming stage.

B. CONTRIBUTIONS

As it was shown in various recent research activities, the deployment of an FC-HBF approach can improve SE compared to the PC case, at the cost however of an increased hardware and computational complexity. To this end, the concept of dynamic subarray formulation can improve performance metrics with reduced computational burden.

However, in all the aforementioned studies, either limited network topologies have been considered (i.e., single cell scenarios), or limited number of active users. Therefore, computational complexity should be evaluated in large-scale deployments. To this end, the novelty of our work can be summarized as follows:

- Development of a system-level simulator for massive MIMO mmWave 5G wireless cellular orientations. As it will be discussed in Section V, results have been extracted when considering orientations with up to two tiers of cells around the central cell.
- Incorporation of the latest 3GPP channel model for 5G orientations in the developed simulator, in an effort to increase the accuracy of the results.
- An adaptive hybrid analog-digital beamforming approach, evaluated in multicellular/multiuser orientations. The key concept of our approach is its low computational complexity. As it will be further explained in Section IV, the complexity is proportional to the number of active users within a cell, which in turn is upper limited by the number of available subcarriers for downlink transmission. This is achieved with the use of a discrete set of beamforming scenarios, able to cover a wide range of MSs' positions. In the same context, each RF chain is connected to a specific subset of transmitting antennas that provide coverage to a specific angular space.
- Utilization of a circular array configuration in order to avoid the deployment of complicated steering mechanisms which would imply additional construction costs and increased complexity among the precoders of the RF chains, thus leading to a non-efficient MIMO architecture.

The rest of this paper is organized as follows: In Section II, the radiating element geometry and the array configuration design is described. The developed simulator setup is analyzed in Section III, along with the channel modelling approach according to 3GPP specifications. In Section IV, the proposed adaptive beamforming approach is described. Simulation results are presented in Section V, where the performance of our proposed adaptive approach for various key performance indicators (KPIs) is highlighted. Finally, concluding remarks and proposals for future work are given in Section VI.

The following notation is used in the paper. An italic variable a or A denotes a scalar, whereas boldface lowercase and uppercase variables \mathbf{a} and \mathbf{A} denote vectors and matrices, respectively. Moreover, $\|\mathbf{a}\|_F$ stands for the Frobenius norm of vector \mathbf{a} . A calligraphic variable \mathcal{A} denotes a set. \mathbf{A}^T and \mathbf{A}^H denote the transpose and conjugate transpose of matrix \mathbf{A} , respectively. Finally, $(\mathbf{A})_{i,j}$ denotes element (i,j) of matrix \mathbf{A} and $\lfloor x \rfloor$ the integer part of x .

II. ANTENNA DESIGN

The proposed adaptive beamformer structure is shown in Fig. 1. At the transmitter side, a baseband digital precoder \mathbf{F}_{BB} processes N_S data streams to produce N_{RF} BS outputs. Throughout the rest of this paper, diversity combining transmission mode is assumed; hence $N_S = K_b$, where the latter term indicates the number of MSs in the b^{th} BS ($1 \leq b \leq B$). However, our approach can be easily extended to the case of spatial multiplexing transmission. \mathbf{F}_{BB} matrix has dimensions $K_b \times \nu$, while each of the ν RF chains is connected to a subset of length w of the total transmitting antennas of a certain vertical array, as shown in Fig. 1. Each one of the multiple transmitting antennas per RF subset is switched to be on or off to form a beam according to the CSI at BSs. This on-off analog beamforming provides reduced hardware and algorithmic complexity. Although this structure corresponds to a PC-HBF architectural case [11], each one of the ν RF chains is intended to provide coverage to a specific angular space. Therefore, the interconnection of all RF chains to all transmitting antennas can be omitted.

Essentially, each RF chain is a vertical array of w crossed dipole (CD) antennas which have been designed to resonate at the mmWave frequency of 28 GHz, as shown in Fig. 2. Besides, the ν RF chains are equally spaced on a ring, ($a=360/\nu$) building a circular array. In particular, each CD antenna consists of two identical but orthogonal ($\pm 45^\circ$) radiating half-wave dipoles, as presented in Fig. 3. It should be noted at this point that the input voltage at the antenna input port is 1V and the phase difference between the half-wave dipoles is 0° , thus formulating a dual polarization (DP) antenna scheme. This is achieved due to the utilization of separate feeding ports. Such type of feeding topologies facilitates the development of the current beamforming-oriented configuration for 5G applications [29]-[32].

In order to enhance the gain in the horizontal plane, as mentioned earlier, each of the vertical crossed dipoles is placed $\lambda/2$ far apart, where λ is the carrier wavelength. To generate unidirectional DP radiation, all the radiating elements are also placed above a perfect electric conductor (PEC, reflector) in a distance of $\sim \lambda/4$, thus leading to a further gain increase. Finally, the width and the spacing between the two radiating elements are of the order of $\lambda/100$, as shown on the right part of Fig. 3 (profile of the CD), [33]-[35].

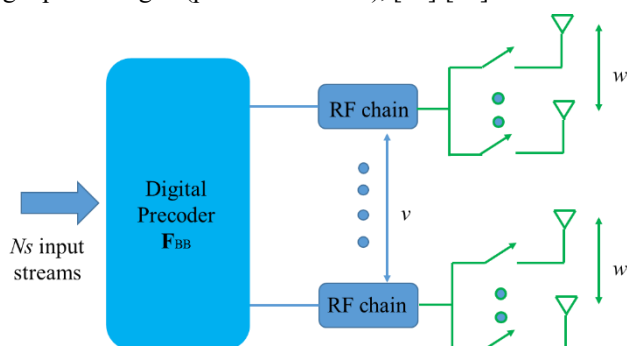


FIGURE 1. Proposed adaptive beamformer structure.

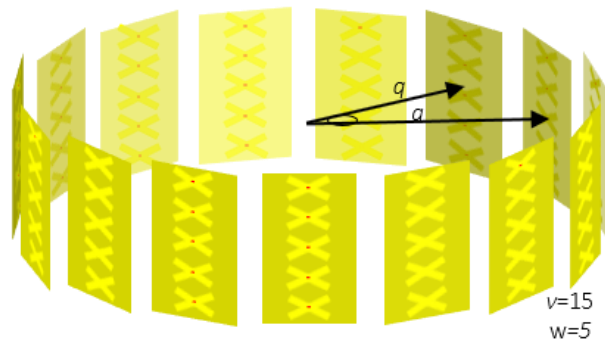


FIGURE 2. An example of circular array. This geometry consists of 15 RF chains and 75 ($\nu \times w$) crossed half-wave dipoles (150 radiating elements) uniformly distributed, $a=360/15=24^\circ$, with a ring radius q .

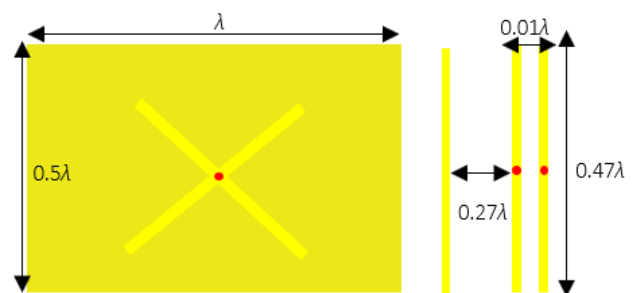


FIGURE 3. Geometry of the reflector using a crossed dipole as an exciter.

The study of the circular array of Fig. 2 in terms of electromagnetic analysis was carried out using the Method of Moments (MoM) [36]. In this context, each study is uniquely characterized by w , q , ν and a parameters. Note that the strong effects of mutual coupling among all the radiating elements ($\nu \times w \times 2$) have been taken into account throughout the current simulations. To this end, the alterations in the radiation pattern and in the input impedance of the array have been considered in our 3D computational model [37].

To begin with, two different sets of simulations will be presented. The first one is characterized by a fixed grid of beams (FGoB) which are excited by a fixed array configuration, characterized by certain q , w , ν and a parameters. On the contrary, in the second set of simulations q and ν values remain constant while a and w values may vary, thus leading to different azimuth radiation patterns, dictating the beamforming technique [38]-[40].

In the FGoB simulations, there are four distinctive array geometries, as shown in Fig. 4, under the parameters of $q=0.149\lambda$, $a=120^\circ$ in Fig. 4(a,b), while $a=45^\circ$ in Fig. 4(c,d). Besides, Fig. 4 provides the gain on the azimuth plane in order to acquire an overview of the radiating beam orientations. As it is expected, an increased number of vertical arrays leads to an increased number of generated beams. In addition, as the number of CDs increases in each vertical array, the maximum gain of the whole array configuration (G_{max}) increases as well.

The G_{max} values are depicted on the column of Fig. 4. It is worth mentioning that the Half Power Beam Width (HPBW) for the array configurations of Fig. 4(a-d) is 70°, 69°, 21° and 21°, respectively.

In the abovementioned case, all the radiating elements are equally excited. An alternate approach for increasing the energy efficiency of the array configuration in terms of improved Quality of Service (QoS) to MSs, is the adaptive beamforming. In this context, the number and the position of the activated CDs are not constant. More specifically, the number of the beams as well as their orientations are dictated by the number and the position of the active MSs, respectively. Hence, certain circular array configurations with constant v , q , a and different w can form beams with different gain and orientation, as shown in Fig. 5. A major feature in the array configuration of Fig. 5 is the number of the initial radiating elements, w_o , which strongly impacts the gain of the whole array in predefined angular locations. In particular, Fig. 5(a) represents an array configuration with $w_o = 4$, $v = 15$, $q = 2.94\lambda$ and $a = 120^\circ$. Depending on the number and the position of the MSs, the circular array configuration of Fig. 5 can rotate either its whole radiation pattern or its beam separately by $\pm 24^\circ$ ($360/v$).

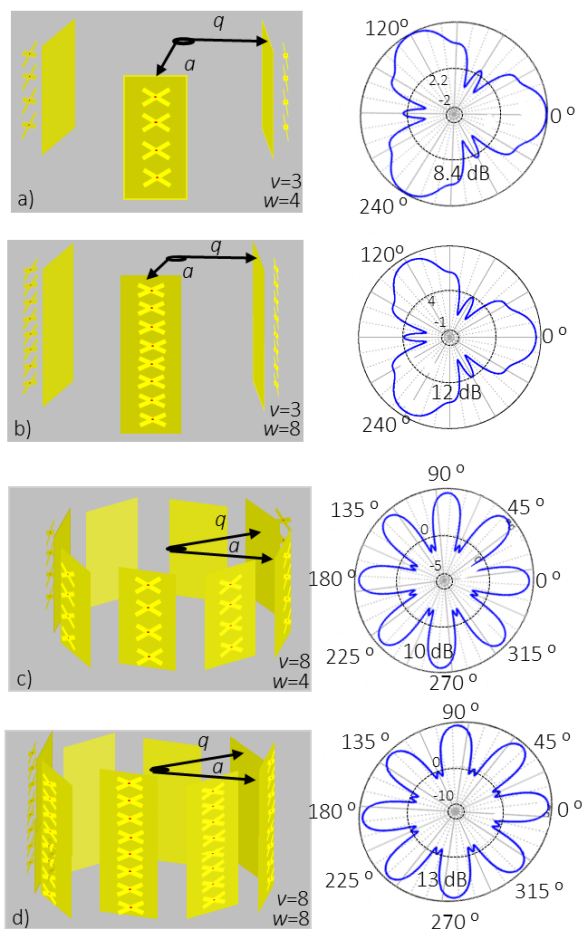


FIGURE 4. Circular array configuration and gain (dB) on the horizontal plane (azimuth) for certain parameters.

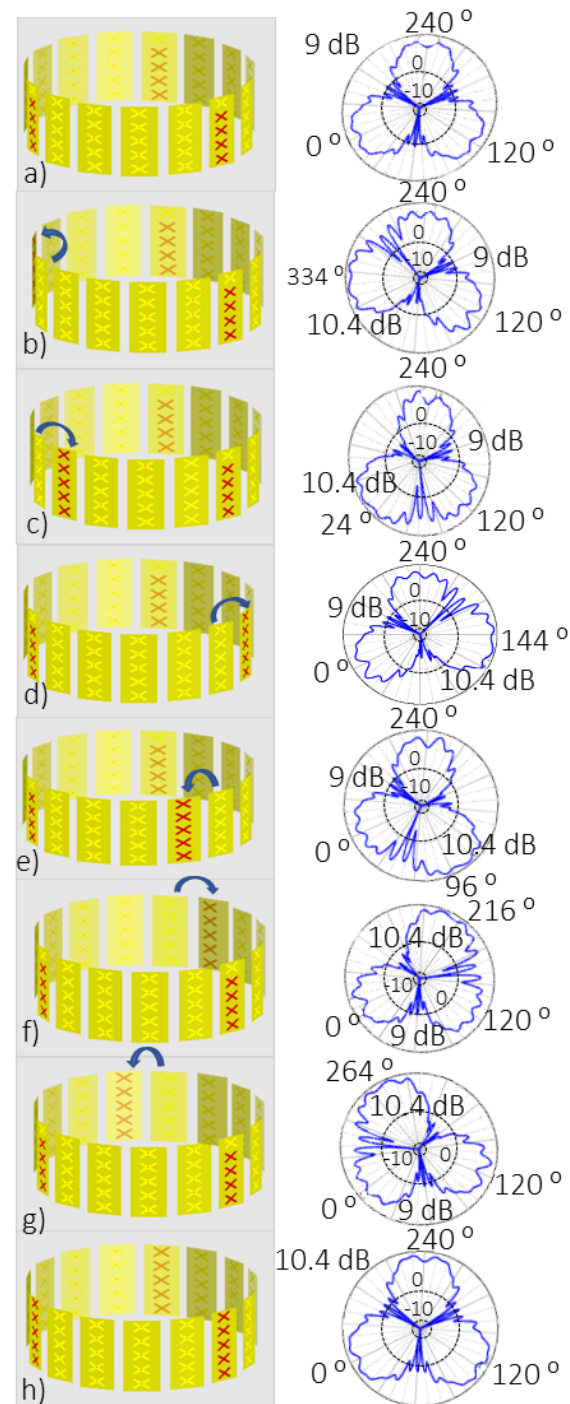


FIGURE 5. Different circular array configurations along with their corresponding horizontal plane beamwidths (azimuth) (the activated CDs are illustrated with red color and angle counting starts from the first activated array on the left, Fig. 5(a), for illustrating purposes).

In case of having an increased number of MSs in a specific angular location, such as Fig. 5(c), the developed array geometry increases $w_o = 4$ to $w = 5$ in the corresponding angle of 24° and preserves w_o to the remaining angles of 120° and 240° (the blue arrows indicate the various activations of vertical arrays with respect to the initial state, as depicted in

Fig. 5(a)). Note here that in the case of $w_o = 4$ then $G_{max} = 9$ dB with $HPBW = 58^\circ$ while for $w = 5$ then $G_{max} = 10.4$ dB with $HPBW = 70^\circ$. Finally, a special case of adaptive beamforming is shown in Fig. 5(h), where w_o increases to $w = 5$ for the whole array configuration, assuming that there is an increase of traffic needs in all predefined angular positions.

It should be mentioned that w can obtain higher values such 10 or 15. However, this would significantly increase the required computational resources along with the duration of the MoM simulations. Hence, the optimum maximum value of w for the purpose of the current work is chosen to be $w = 5$. Finally, the array configuration with its corresponding horizontal plane beamwidths (Fig. 5), which are defined each time by the activated vertical arrays, suggests a multifunctional array scheme with extremely low-cost and low-complexity hardware. In this context, the activation of certain number of vertical arrays in a specific angular position without any steering mechanism, can significantly simplify the design and implementation of the current broadband wireless network.

III. SIMULATION SETUP

A 5G system-level simulator has been developed (OFDMA transmission), executing independent Monte Carlo (MC) simulations in parallel. To this end, MSs are uniformly distributed in a two-tier wireless cellular orientation. Each MS requests R_k Mbps ($1 \leq k \leq K$) from its serving BS that can be potentially fulfilled by a proper assignment of Physical Resource Blocks (PRBs) and modulation order per PRB [41].

The goal of subcarrier allocation and adaptive beamforming that will be described in the following section is to maximize overall throughput with minimum downlink transmission power and blocking probability (BP). Thus, the optimization problem (P) may be formulated as follows:

$$\begin{aligned} & \max R_k, \quad 1 \leq k \leq K \\ & \min \sum_{s \in \mathcal{S}_k} p_{k,s}, \quad 1 \leq k \leq K \\ & \min BP \\ & \text{s.t.: (C1)} \quad \sum_{k=1, k \in \mathcal{MS}_b}^K \sum_{s \in \mathcal{S}_k} p_{k,s} \leq P_m, \quad 1 \leq b \leq B \quad (1) \\ & \text{(C2)} \quad \sum_{s \in \mathcal{S}_k} p_{k,s} \leq p_m, \quad 1 \leq k \leq K \\ & \text{(C3)} \quad \sum_{k=1, k \in \mathcal{MS}_b}^K |\mathcal{S}_k| \leq N_{PRB}, \quad 1 \leq b \leq B \end{aligned}$$

where $p_{k,s}$ is the downlink transmission power per allocated PRB for the k^{th} MS and \mathcal{S}_k the corresponding set of allocated PRBs. Moreover, $|\mathcal{S}_k|$ is the length of set \mathcal{S}_k , \mathcal{MS}_b denotes the set of active MSs in the b^{th} BS and N_{PRB} denotes the available PRBs per BS. Finally, BP is defined as the number of MSs that were not granted access to the network to the total number of MSs.

According to the first two constraints, downlink transmission power per BS/MS should not exceed a predefined threshold. The final constraint indicates that hard blocking may occur in case of lack of available PRBs in one of the active BSs. The new MS is admitted in the network provided that acceptable QoS can be guaranteed without power excess in one of the BSs. Note that during an MC run, the positions of the MSs as well as corresponding system-level parameters (i.e., pathloss, channel coefficients, etc.), remain unchanged. Each MC run comes to an end either when excess of power or lack of available PRBs is triggered in at least one of the active BSs.

For every potential (new) MS, pathloss calculation takes place according to the urban macro-cellular (UMa) model, while channel coefficients generation is performed according to the latest 3GPP channel model [42]. In this context, for an arbitrary pair of Tx-Rx each channel is modelled as a sum of equivalent channels from N clusters, where each one is further decomposed to M subpaths. Considering a non-line of sight (NLOS) environment, the channel impulse response for an arbitrary pair of transmitting-receiving antennas (denoted as q and u , respectively) is given by [42]:

$$H_{u,q}^{\text{NLOS}}(\tau, t) = \sum_{n=1}^2 \sum_{i=1}^3 \sum_{m \in \mathcal{R}_i} H_{u,q,n,m}^{\text{NLOS}}(t) \delta(t - \tau_{n,i}) + \sum_{n=3}^N H_{u,q,n}^{\text{NLOS}}(t) \delta(t - \tau_n) \quad (2)$$

where $\tau_{n,i}$, τ_n represent the delay of the i^{th} subcluster of the n^{th} cluster and the delay of the n^{th} cluster, respectively, and δ stands for the Kronecker delta. It is important to note at this point that for the first two dominant clusters three additional sub-clusters are defined. The subpaths per sub-cluster are stored in set \mathcal{R}_i . Moreover, $H_{u,q,n}^{\text{NLOS}}$ and $H_{u,q,n}^{\text{NLOS}}$ are given by:

$$H_{u,q,n,m}^{\text{NLOS}} = \sqrt{\frac{P}{M}} \mathbf{F}_{rx,n,m}^T \mathbf{\Theta}_{n,m} \mathbf{F}_{tx,n,m} \exp\left(\frac{j2\pi(\hat{\mathbf{r}}_{rx,n,m}^T \cdot \bar{\mathbf{d}}_{rx,u})}{\lambda}\right) \exp\left(\frac{j2\pi(\hat{\mathbf{r}}_{tx,n,m}^T \cdot \bar{\mathbf{d}}_{tx,q})}{\lambda}\right) \quad (3)$$

$$H_{u,q,n}^{\text{NLOS}} = \sum_{m=1}^M H_{u,q,n,m}^{\text{NLOS}} \quad (4)$$

where:

$$\mathbf{F}_{rx,n,m} = \begin{bmatrix} F_{rx,u,\theta}(\theta_{n,m,ZOA}, \phi_{n,m,AOA}) \\ F_{rx,u,\phi}(\theta_{n,m,ZOA}, \phi_{n,m,AOA}) \end{bmatrix} \quad (5)$$

$$\mathbf{F}_{tx,n,m} = \begin{bmatrix} F_{tx,q,\theta}(\theta_{n,m,ZOD}, \phi_{n,m,AOD}) \\ F_{tx,q,\phi}(\theta_{n,m,ZOD}, \phi_{n,m,AOD}) \end{bmatrix} \quad (6)$$

$$\mathbf{\Theta}_{n,m} = \begin{bmatrix} \exp(j\Phi_{n,m}^{\theta\theta}) & \sqrt{\kappa_{n,m}^{-1}} \exp(j\Phi_{n,m}^{\theta\phi}) \\ \sqrt{\kappa_{n,m}^{-1}} \exp(j\Phi_{n,m}^{\phi\theta}) & \exp(j\Phi_{n,m}^{\phi\phi}) \end{bmatrix} \quad (7)$$

In the above set of equations, $\theta_{n,m,ZoD}$ and $\theta_{n,m,ZoA}$ represent the angles of departure (AoD) and arrival (AoA), respectively, in the vertical plane for the m^{th} subpath ($1 \leq m \leq M$) of the n^{th} cluster ($1 \leq n \leq N$). The corresponding parameters for the horizontal plane are $\phi_{n,m,AoD}$ and $\phi_{n,m,AoA}$, respectively. Moreover, P_n is the power of the n^{th} cluster, set $\{\Phi_{n,m}^{\theta\theta}, \Phi_{n,m}^{\theta\phi}, \Phi_{n,m}^{\phi\theta}, \Phi_{n,m}^{\phi\phi}\}$ corresponds to initial phases uniformly distributed in $(-\pi, \pi)$ while $\kappa_{n,m}$ parameter is the generated cross polarization power ratio (XPR) for each ray m of cluster n . In addition, $\hat{r}_{rx,n,m}$ is the spherical unit vector with azimuth arrival angle $\phi_{n,m,AoA}$ and elevation arrival angle $\theta_{n,m,ZoA}$, while $\hat{r}_{tx,n,m}$ is the spherical unit vector with azimuth departure angle $\phi_{n,m,AoD}$ and elevation departure angle $\theta_{n,m,ZoD}$. Moreover, $\mathbf{F}_{tx}/\mathbf{F}_{rx}$ represent the field pattern of transmitting/receiving antenna element q/u , respectively ($1 \leq q \leq N_t$, $1 \leq u \leq N_r$), $\mathbf{d}_{rx,u}$ is the location vector of receive antenna element u and $\mathbf{d}_{tx,q}$ is the location vector of transmit antenna element q . Note here that the values of the former variables of \mathbf{F}_{tx} , \mathbf{F}_{rx} are calculated through MoM, as mentioned in the previous section. Finally, j is the imaginary unit.

As it will be shown in the results section, for each deployed massive MIMO configuration three KPIs are derived: Total network throughput (Mbps), total downlink transmission power (W), as well as BP.

IV. ADAPTIVE BEAMFORMING IN MASSIVE MIMO SYSTEMS

A. PROPOSED APPROACH

The studied adaptive beamforming approach is described in Table I. In this context, the set \mathcal{RE}_b denotes the active radiating elements of the array geometry deployed in the b^{th} BS and \mathcal{AB}_b the corresponding angles of the generated adaptive beams (notation $a:b$ indicates all elements from a to b with step 1). Moreover, each entry of $\mathbf{H}_{k,\text{sec}(k),s}$ (indicating the channel matrix of the k^{th} MS relevant to its serving sector for the s^{th} PRB) is calculated according to (2). In addition, \mathbf{x} represents the eigenvector corresponding to the maximum eigenvalue of matrix $\mathbf{H}_{k,\text{sec}(k),s}^H \mathbf{H}_{k,\text{sec}(k),s}$, SNR_k is the signal to noise ratio of the k^{th} MS with respect to all available PRBs of the b^{th} BS (i.e., \mathcal{S}_b) and $TL_{k,\text{sec}(k),s}$, $CG_{k,s}$ represent the total losses and the channel gain, respectively, of the k^{th} MS relevant to the s^{th} PRB. Finally, the minimum required SNR for acceptable QoS and the thermal noise level at the receiver are denoted by SNR_{th} and I_o , respectively. Note that during subcarrier allocation (line 3), function $\text{sort}(\text{SNR}_k, R_k)$ sorts the values in vector matrix SNR_k in descending order and returns the first R_k sorted values as well as the corresponding indexes (assigned to set \mathcal{S}_k).

TABLE I

The Proposed Adaptive Beamforming Approach	
1:	$\mathcal{RE}_b \leftarrow \left\{ (v_o, 1: w_o), \left(v_o + \left\lceil \frac{v}{3} \right\rceil, 1: w_o \right), \left(v_o + 2 \left\lceil \frac{v}{3} \right\rceil, 1: w_o \right) \right\}$
$\mathcal{AB}_b \leftarrow \{F_0, F_1, F_2\}$, $L_b \leftarrow \mathcal{AB}_b $, $\mathcal{S}_b \leftarrow \{1: N_{PRB}\}$, $1 \leq b \leq B$, $k \leftarrow 1$	
2:	$k \leftarrow k+1$. The k^{th} MS tries to access the network in the b^{th} BS requesting R_k PRBs (φ_k is the angle with respect to the horizontal plane)
3:	$[\text{SNR}_k, \mathcal{S}_k] \leftarrow \text{sort}(\text{SNR}_k, R_k)$
4:	for every $s \in \mathcal{S}_k$
5:	$\mathbf{t}_{k,s} \leftarrow \mathbf{x} \left(\lambda_m \left(\mathbf{H}_{k,\text{sec}(k),s}^H \mathbf{H}_{k,\text{sec}(k),s} \right) \right)$
6:	$CG_{k,s} \leftarrow \left\ \mathbf{H}_{k,\text{sec}(k),s}^H \right\ _F^2 / TL_{k,\text{sec}(k),s}$, $p_{k,s} \leftarrow (\text{SNR}_{th} \cdot I_o) / CG_{k,s}$
7:	end for
8:	$\{l, \tilde{v}_k\} \leftarrow \underset{F_l \in \mathcal{AB}_b}{\text{argmin}} \varphi_k - F_l $
9:	if $\sum_{s \in \mathcal{S}_k} p_{k,s} \geq p_m$ then
10:	$\mathcal{RE}_b \leftarrow \mathcal{RE}_b - \{(\tilde{v}_k, 1: w_o)\}$
11:	if $\varphi_k > F_l$ then $\tilde{v}_k \leftarrow \tilde{v}_k + 1$, $\mathcal{RE}_b \leftarrow \mathcal{RE}_b + \{(\tilde{v}_k, 1: w)\}$
12:	else
13:	$\tilde{v}_k \leftarrow \tilde{v}_k - 1$, $\mathcal{RE}_b \leftarrow \mathcal{RE}_b + \{(\tilde{v}_k, 1: w)\}$
14:	end if
15:	Recalculate $\mathbf{H}_{k',\text{sec}(k),s}$, $\mathbf{t}_{k',s}$, $CG_{k',s}$, $p_{k',s}$ for every $k' \in \mathcal{MS}_b$, $s \in \mathcal{S}_k$.
16:	if $\sum_{s \in \mathcal{S}_k} p_{k',s} \geq p_m$ for an arbitrary $k' \in \mathcal{MS}_b$, then
17:	Restore $\mathbf{H}_{k',\text{sec}(k),s}$, $\mathbf{t}_{k',s}$, $CG_{k',s}$, $p_{k',s}$ for every $k' \in \mathcal{MS}_b$, $s \in \mathcal{S}_k$.
18:	$\mathcal{RE}_b \leftarrow \mathcal{RE}_b - \{(\tilde{v}_k, 1: w)\}$
19:	$\mathcal{RE}_b \leftarrow \left\{ (v_o, 1: w), \left(v_o + \left\lceil \frac{v}{3} \right\rceil, 1: w \right), \left(v_o + 2 \left\lceil \frac{v}{3} \right\rceil, 1: w \right) \right\}$
20:	Recalculate $\mathbf{H}_{k',\text{sec}(k),s}$, $\mathbf{t}_{k',s}$, $CG_{k',s}$, $p_{k',s}$ for every $k' \in \mathcal{MS}_b$, $s \in \mathcal{S}_k$.
21:	if $\sum_{s \in \mathcal{S}_k} p_{k',s} \geq p_m$ for an arbitrary $k' \in \mathcal{MS}_b$, then
22:	$rf \leftarrow 1$
23:	$\mathcal{RE}_b \leftarrow \left\{ (v_o, 1: w_o), \left(v_o + \left\lceil \frac{v}{3} \right\rceil, 1: w_o \right), \left(v_o + 2 \left\lceil \frac{v}{3} \right\rceil, 1: w_o \right) \right\}$
24:	Restore $\mathbf{H}_{k',\text{sec}(k),s}$, $\mathbf{t}_{k',s}$, $CG_{k',s}$, $p_{k',s}$ for every $k' \in \mathcal{MS}_b$, $s \in \mathcal{S}_k$.
25:	end if
26:	else
27:	$rf \leftarrow 0$
28:	end if (line 16)
29:	else
30:	$rf \leftarrow 0$
31:	end if (line 9)
32:	if $rf = 0$, then
33:	$\mathcal{S}_b \leftarrow \mathcal{S}_b - \mathcal{S}_k$, $\mathcal{MS}_b \leftarrow \mathcal{MS}_b \cup k$
34:	Set $P_{t,b} \leftarrow P_{t,b} + \sum_{s \in \mathcal{S}_k} p_{k,s}$ (transmit power of the b^{th} BS)
35:	if $P_{t,b} > P_m$ or $ \mathcal{S}_b < R_k$ then MC simulation terminates, else go
36:	to Step 2
37:	end if
38:	else go to Step 2
39:	end if

In the initial state, it is assumed that an arbitrary BS employs a FGoB, where three active sectors have a spatial separation of 120° (e.g., Fig. 5(a)). To this end, the deployed geometry is defined according to the angle of the first MS which is served by this BS. Assuming that in this case the vertical array v_o is activated, then two additional arrays, and in particular $v_o + [v/3]$ and $v_o + 2[v/3]$ are activated as well, in order to provide the necessary 120° separation in the deployed beams. Once a potential (new) MS requesting R_k PRBs tries to enter the network, it is examined if the minimum required transmission power for acceptable QoS can be provided from the already deployed geometry without power outage. If this is true, then this MS is accepted in the network and all equivalent parameters are updated (MS is served by the l^{th} beam which is generated by the \tilde{v}_k vertical array, line 8). However, in the opposite case (line 9), the beam can be steered to an adjacent angular location (e.g., Fig. 5(b - g)). This is achieved by the activation of a different vertical array, according to the angular position of the potential new MS (lines 11-14 in Table I and blue arrows in Fig. 5 that indicate the adjacent vertical arrays). Note that in this case all radiating elements of this array are activated. If however power outage occurs in at least one of the already served MSs of this BS, then all radiating elements in the initial vertical arrays (as defined in line 1) can be activated, thus providing a grid of beams with increased gain (Fig. 5(h), line 19 in Table I).

In all the aforementioned cases where antenna radiation pattern modification takes place, it is examined if the considered alterations in the radiation diagram will result in link outage for another of the already served MSs by the b^{th} BS (e.g., lines 16 and 21), as it was previously explained. If this is true even in the case where all radiating elements per vertical array are activated (Fig. 5(h)), or the considered MS cannot be provided with acceptable QoS, then reject flag (rf) is set to 1 and the process is repeated for the next candidate MS. Otherwise, corresponding sets (i.e., \mathcal{S}_b and \mathcal{MS}_b) are updated. Finally, as also mentioned in Section II, each MC run comes to an end either when the transmission power of the b^{th} BS (denoted as $P_{t,b}$) exceeds a predefined threshold (P_m) or lack of available PRBs takes place.

B. COMPLEXITY-CONVERGENCE

According to [26], for an MU downlink system with N_{RF} RF chains and N_t transmitting antennas, the computational complexity of optimum antenna partitioning will be given by

$$\frac{1}{(N_{RF})!} \sum_{k=0}^{N_{RF}} (-1)^{N_{RF}-k} \binom{N_{RF}}{k} k^{N_t} \quad (8)$$

This complexity can be significant, even for a small number of RF chains and antennas. In [26], the complexity of the proposed subarray partitioning algorithm is reduced to $N_{RF} \times N_t$. In [28], the complexity of various analogic beamforming algorithms is evaluated, which is proved to be of the order of $O(N_t^3)$.

In the same context, in the HBF approach of [23], complexity is of the order of $O(N_{RF} \times 2^B)$, where B is the number of bits of the low-resolution phase shifters. Moreover, in [19], where the OFDM-based HBF is studied, corresponding complexity is of the order of $O(K \times N_t^2)$, where K is the number of active MSs. Therefore, even for a moderate number of transmitting antennas, computational complexity can be significantly increased.

As it is apparent from the description of the previous subsection where the proposed adaptive beamforming algorithm of Table I is described, in the worst-case scenario two beamforming modifications in the BS's radiation pattern will take place: In lines 11-14, where a beam is steered towards the direction of the new potential MS, as well as in line 19, where now all radiating elements of all vertical arrays are activated. Since transmission precoding vectors as well as assigned PRBs are calculated on MS entry (lines 4-7), the complexity of the proposed beamforming approach is proportional to the number of active MSs within the specific BS (the decision on beampattern modification is based on the sum of the calculated downlink transmission powers), which, in turn, is upper limited by the number of available PRBs per BS.

Moreover, as it was previously explained, if during beampattern modification downlink power outage occurs in at least one of the active MSs, then either a new beamforming modification will take place or, eventually, rejection of the new MS. Therefore, at the end of each repetition of the steps in Table I, three possible events may occur: MS entry with/without beampattern modification as well as MS rejection. Hence, the convergence of our proposed approach is always guaranteed, since its deployment is based on a predefined set of radiation diagrams which in turn is achieved with a simple on-off activation of radiating elements per vertical array.

V. RESULTS

A. FIXED GRID OF BEAMS PER BS

The first set of simulation results is presented in Figs. 6-8 for the considered antenna geometries of Fig.4 (FGoB). In all figures, cumulative distribution function (CDF) curves have been plotted versus each of the considered KPIs of Section II. Since adaptive modulation and coding per subcarrier is outside the scope of our study, we consider two distinct values for the requested transmission rate, common for all MSs (i.e., $R_k = R$), which is can be satisfied with a proper assignment of PRBs and modulation order per PRB. In this context, in all simulation scenarios either 5 or 15 PRBs can be allocated to a potential MS, thus equivalent bit rates of 7.2/21.6 Mbps can be supported (i.e., the product of the assigned PRBs per MS, the subcarriers per PRB, the subcarrier spacing, as well the transmitted bits per subcarrier as defined by the modulation type - Table II).

TABLE II
SIMULATION PARAMETERS

Parameter	Value/Assumption
Tiers of cells	2
Pathloss model	UMa
Carrier frequency (GHz)	28
Channel Bandwidth (MHz)	100
Subcarrier spacing (kHz)	60
Subcarriers per PRB	12
Cell radius (m)	500
Assigned PRBs per MS	5/15
Monte Carlo snapshots per scenario	10^4
Required E_b/N_0 (dB)	9.6 [43]
Maximum transmission power per BS/MS (W)	20/1
Considered antenna geometries at BSs ($v \times w$)	3×4 , 3×8 , 8×4 , 8×8 , 15×5
Antenna elements per MS	2
Transmission mode	Diversity Combining

Moreover, wireless orientations with two tiers of cells around the central cell have been considered. All simulation parameters are summarized in Table II, which are aligned with the majority of related works in [44]. Finally, in each figure legend, notation (v, w, R) has been considered. Since all vertical arrays are activated, the term active beams will be used as well throughout the rest of this subsection to indicate the number of generated beams per BS.

As it can be observed from Fig. 6, throughput is maximized for 5 PRBs per MS, four radiating elements per vertical array and three/eight active beams per BS (the group of two curves in the right part of Fig. 1). It is interesting to note that there is a throughput reduction when eight radiating elements are deployed per vertical array, compared to the previous cases. In this case, on one hand the increased number of radiating elements increases spatial directivity, but on the other, leads to reduced spatial coverage. In all cases throughput is reduced for 15 PRBs per MS, as expected, since high data rate services can be supported for a limited number of active MSs. As in the previous case of 5 PRBs per MS, throughput is maximized when considering a limited number of CDs per vertical array.

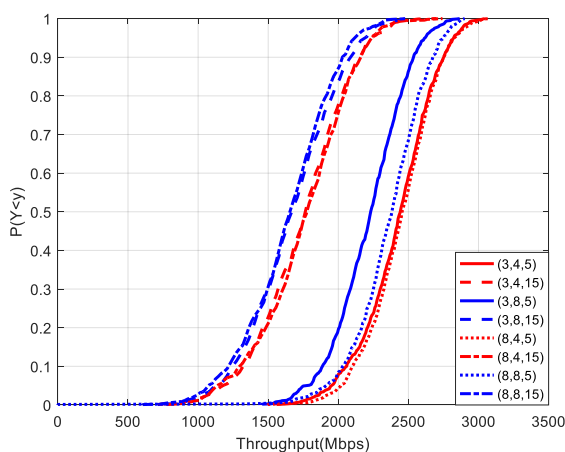


FIGURE 6. Total network throughput (Mbps).

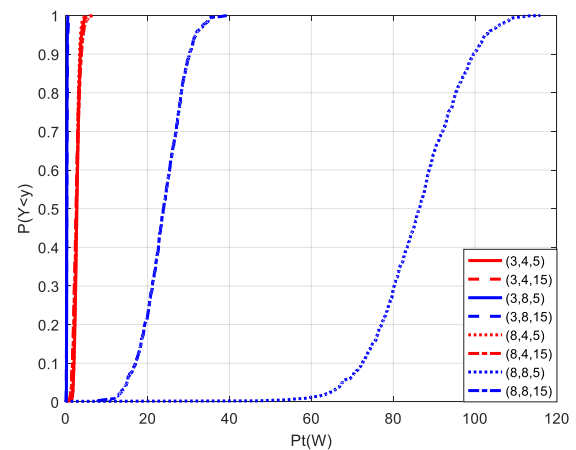


FIGURE 7. Total transmission power (W).

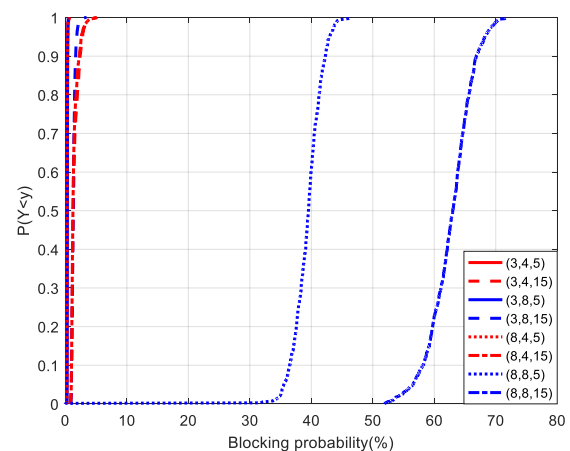


FIGURE 8. Blocking probability (%).

In Fig. 7, CDF curves of total downlink transmission power are depicted. Transmission power is maximized for five PRBs per MS, eight CDs per vertical array and eight beams per BS. In this case, taking into consideration that for this specific scenario median BP is almost 30% (Fig. 8), a greater amount of transmission power is required to compensate for the reduced spatial coverage of this configuration. In the cases of four CDs per vertical array (5/15 PRBs per MS and three/eight active beams), then both BP and total downlink transmission power are minimized.

Therefore, it becomes apparent from the above that the generation of highly directional beams in predefined angular locations can lead to downlink transmission power increase and BP degradation, due to the reduced spatial coverage. For this reason, in the following subsection the antenna geometry of Fig. 5 has been considered, where in each MC snapshot and depending on MSs' distribution three active beams are generated. Thus, the necessary spatial coverage is provided around 360° , which in turn depends on the orientation of the activated vertical arrays as well as on the number of the activated CDs per vertical array. Both the aforementioned parameters are primarily defined according to traffic needs.

B. ADAPTIVE GRID OF BEAMS

In the second set of simulation results (Figs. 9-12), the proposed adaptive beamforming approach has been considered. To this end, the geometry of Fig. 5 is deployed in each one of the active BSs. All output metrics are compared against the FGoB scenario, where three beams per BS at $\{0^\circ, 120^\circ, 240^\circ\}$ are generated. In Fig. 12, an additional KPI is taken into consideration: the total number of radiating elements per MC simulation in the adaptive grid of beams (AGoB) and FGoB scenarios. In all figures, notation (v, w, R) is used when considering the FGoB (also depicted as FB) while notation (v, w, w_o, R) is used for the AGoB (also depicted as AB). Throughout the rest of this analysis, unless otherwise specified, all KPIs are compared with respect to their mean values.

As it can be observed from Fig. 9, there are no significant throughput variations in the AGoB and FGoB cases for all the considered MIMO configurations. However, as it is evident from Fig. 12, a significant reduction in the total number of radiating elements can be achieved. Considering 5 PRBs per MS and $w_o = 3$ in the AGoB scenario, a mean total throughput of 2245 Mbps can be supported, as in the FGoB case. However, 190 radiating elements are now activated versus 285 elements in the FGoB case. This value is further increased to 230, when $w_o = 4$. Nevertheless, this increment is combined with reduced transmission power compared to the $w_o = 3$ case. In particular, corresponding mean values are (17/10) W, respectively, for the aforementioned scenarios ($w_o = 3, 4$). In the case of 15 PRBs per MS, a total network throughput of 1700 Mbps can be supported. Active radiating elements are now 182/223/277 for the considered three cases (AGoB with $w_o = 3, 4$, respectively, and FGoB) while corresponding transmission power is 9/6/4.8 W. In addition, when $w_o = 4$ then BP can be reduced compared to the FGoB approach: for 5 PRBs per MS corresponding values are 0.75%/0.5% for the FGoB/AGoB cases, respectively, and 3.8%/2.5% when considering 15 PRBs per MS.

It is important to note at this point that there is a trade-off between hardware complexity reduction (expressed via the reduced number of radiating elements) and total downlink transmission power, since in the FGoB case mean transmission power is reduced compared to the AGoB case. For this reason, an additional MIMO configuration has been considered, where now $w_o = w = 5$. Apparently, for this scenario the number of active RF chains will be similar for the two considered cases (fixed and adaptive beams). However, as it is evident from Fig. 10, overall transmission power for 5 PRBs per MS is reduced in the AGoB scenario (6.3 W) when compared with the FGoB case (7 W). Corresponding values are 4.2/4.8 W, respectively, when considering 15 PRBs per MS. Similar conclusions can be drawn for BP as well, since it is further reduced to 0.4%/2.1% for 5/15 PBRs per MS, respectively.

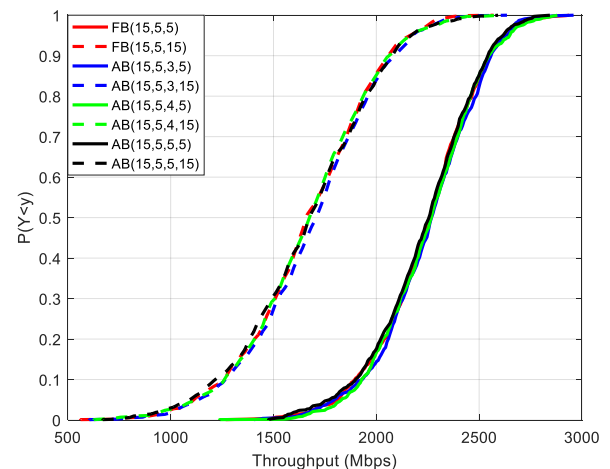


FIGURE 9. Total network throughput (Mbps).

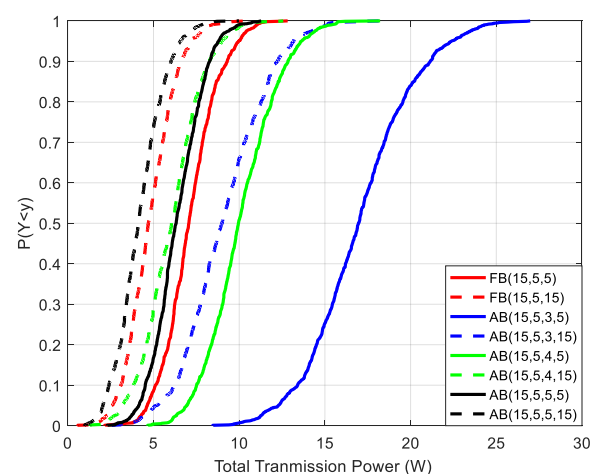


FIGURE 10. Total transmission power (W).

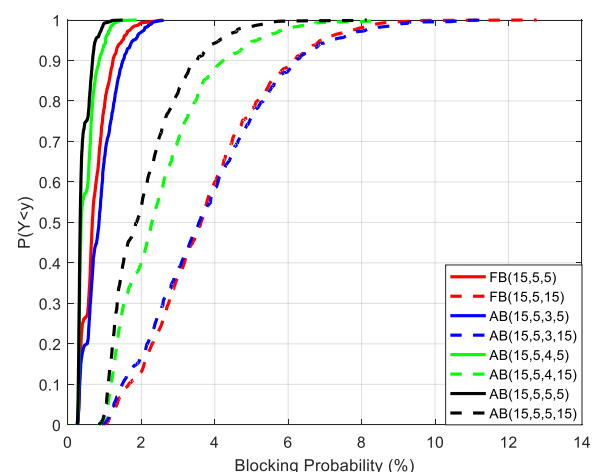


FIGURE 11. Blocking probability (%).

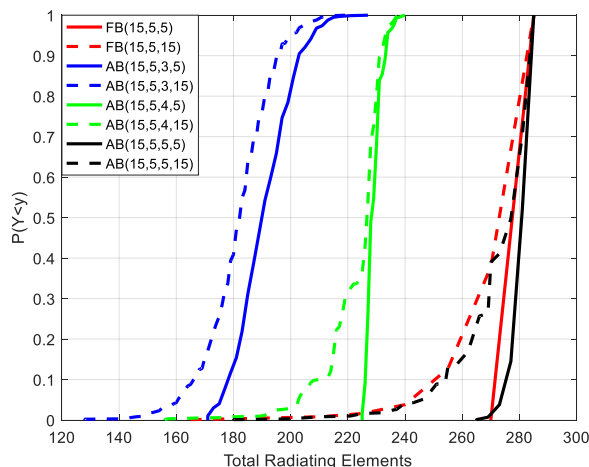


FIGURE 12. Active radiating elements.

VI. CONCLUSIONS

The performance of an adaptive hybrid beamforming approach in the context of 5G mmWave cellular networks has been evaluated. In this context, a separate RF chain is connected per vertical antenna array and radiation pattern formulation is performed via the activation of a different set of antenna elements. Each vertical array constitutes a radiating element of a circular array configuration facilitating a broad spatial coverage around 360°.

According to the presented results, although hardware complexity reduction (expressed via the number of active radiating antenna elements) comes at the cost of increased transmission power, our adaptive beamforming approach can improve various KPIs of the cellular orientation, such as total downlink transmission power when all radiating elements per vertical antenna array are activated, as well as blocking probability. It should be noted at this point that the proposed adaptive beamforming scheme is based on perfect CSI at BSs. However, our approach can be easily extended to the case where the analog stage employs codebook searching to avoid channel estimation of the analog channel with large dimensions.

Future work includes among others the extension of the presented approach in more demanding user traffic scenarios (e.g., formulation of user-specific directive beams) as well as in distributed MIMO architectures. To this end, the derived conclusions of the current work can be applied in more efficient array configurations, in terms of obtained directivity and physical size, employing chip scale radiating elements. In this context, the study of smart antennas as well as the research of plasmonic nanoantennas aiming at optical frequencies can lead the way to the forthcoming era of 6G applications.

ACKNOWLEDGMENT

This work has been partially supported by the Affordable5G project, funded by the European Commission under Grant Agreement H2020-ICT-2020-1, number 957317 through the Horizon 2020 and 5G-PPP programs (www.affordable5g.eu/).

REFERENCES

- [1] Y. Xu, G. Gui, H. Gacanin and F. Adachi, "A survey on resource allocation for 5G heterogeneous networks: Current research, future trends, and challenges," *IEEE Commun. Surv. Tutor.*, vol. 23, no. 2, pp. 668-695, Secondquarter 2021.
- [2] A. N. Uwaechia and N. M. Mahyuddin, "A comprehensive survey on millimeter wave communications for fifth-generation wireless networks: Feasibility and challenges," *IEEE Access*, vol. 8, pp. 62367-62414, Mar. 2020.
- [3] A. V. Lopez, A. Chervyakov, G. Chance, S. Verma and Y. Tang, "Opportunities and challenges of mmWave NR," *IEEE Wirel. Commun.*, vol. 26, no. 2, pp. 4-6, Apr. 2019.
- [4] B. Makki, K. Chitti, A. Behravan and M. -S. Alouini, "A survey of NOMA: Current status and open research challenges," *IEEE OJ-COMS*, vol. 1, pp. 179-189, Jan. 2020.
- [5] N. Nomikos, E. T. Michailidis, P. Trakadas, D. Vouyioukas, T. Zahariadis and I. Krikidis, "Flex-NOMA: Exploiting buffer-aided relay selection for massive connectivity in the 5G uplink," *IEEE Access*, vol. 7, pp. 88743-88755, Jul. 2019.
- [6] E. G. Larsson, O. Edfors, F. Tufvesson and T. L. Marzetta, "Massive MIMO for next generation wireless systems," *IEEE Commun. Mag.*, vol. 52, no. 2, pp. 186-195, Feb. 2014.
- [7] H. Ji et al., "Overview of full-dimension MIMO in LTE-advanced pro," *IEEE Commun. Mag.*, vol. 55, no. 2, pp. 176-184, Feb. 2017.
- [8] A. Ghosh, A. Maeder, M. Baker and D. Chandramouli, "5G evolution: A view on 5G cellular technology beyond 3GPP release 15," *IEEE Access*, vol. 7, pp. 127639-127651, Sept. 2019.
- [9] E. Calvanese Strinati et al., "6G: The next frontier: From holographic messaging to artificial intelligence using subterahertz and visible light communication," *IEEE Veh. Technol. Mag.*, vol. 14, no. 3, pp. 42-50, Sept. 2019.
- [10] P. Schulz et al., "Latency critical IoT applications in 5G: Perspective on the design of radio interface and network architecture," *IEEE Commun. Mag.*, vol. 55, no. 2, pp. 70-78, Feb. 2017.
- [11] A. F. Molisch et al., "Hybrid beamforming for massive MIMO: A survey," *IEEE Commun. Mag.*, vol. 55, no. 9, pp. 134-141, Sept. 2017.
- [12] J. Zhang, X. Yu and K. B. Letaief, "Hybrid beamforming for 5G and beyond millimeter-wave systems: A holistic view," *IEEE OJ-COMS*, vol. 1, pp. 77-91, Dec. 2019.
- [13] S. S. Ioushua and Y. C. Eldar, "A family of hybrid analog-digital beamforming methods for massive MIMO systems," *IEEE Trans. Signal Proces.*, vol. 67, no. 12, pp. 3243-3257, Jun. 2019.
- [14] S. Zhang, C. Guo, T. Wang and W. Zhang, "ON-OFF analog beamforming for massive MIMO," *IEEE Trans. on Veh. Tech.*, vol. 67, no. 5, pp. 4113-4123, May 2018.
- [15] M. Soleimani, R. C. Elliott, W. A. Krzymień, J. Melzer and P. Mousavi, "Hybrid beamforming for mmWave massive MIMO systems employing DFT-assisted user clustering," *IEEE Trans. on Veh. Tech.*, vol. 69, no. 10, pp. 11646-11658, Oct. 2020.
- [16] A. Ferreira, G. Gaspar, P. Montezuma, R. Dinis and N. Jayakody, "A power efficient technique for double layer massive MIMO schemes," *IEEE 86th Veh. Tech. Conf. (VTC-Fall)*, Toronto, Canada, 24-27 Sep. 2017, pp. 1-6, DOI: 10.1109/VTCFall.2017.8288135.
- [17] Z. C. Phyo and A. Taparugssanagorn, "Hybrid analog-digital downlink beamforming for massive MIMO system with uniform and non-uniform linear arrays," *13th International Conference on Electrical Engineering/Electronics, Computer, Telecommunications and Information Technology (ECTI-*

- CON), Chiang Mai, Thailand, Jun. 28-Jul. 1 2016, pp. 1-6, DOI: 10.1109/ECTICon.2016.7561395.
- [18] M. S. Aljumaily and H. Li, "Machine learning aided hybrid beamforming in massive-MIMO millimeter wave systems," *IEEE International Symposium on Dynamic Spectrum Access Networks (DySPAN)*, Newark, NJ, USA, 11-14 Nov. 2019, pp. 1-6, DOI: 10.1109/DySPAN.2019.8935814.
 - [19] F. Sohrabi and W. Yu, "Hybrid analog and digital beamforming for mmWave OFDM large-scale antenna arrays," *IEEE J. Sel. Areas Commun.*, vol. 35, no. 7, pp. 1432-1443, Jul. 2017.
 - [20] J. Tao, J. Xing, J. Chen, C. Zhang and S. Fu, "Deep neural hybrid beamforming for multi-user mmWave massive MIMO system," *7th IEEE Global Conf. on Signal and Inf. Processing (GlobalSIP)*, Ottawa, Ontario, Canada, 11-14 Nov. 2019, pp. 1-5, DOI: 10.1109/GlobalSIP45357.2019.8969154.
 - [21] D. Castanheira, P. Lopes, A. Silva and A. Gameiro, "Hybrid beamforming designs for massive MIMO millimeter-wave heterogeneous systems," *IEEE Access*, vol. 5, pp. 21806-21817, Oct. 2017.
 - [22] X. Wu, D. Liu and F. Yin, "Hybrid beamforming for multi-user massive MIMO systems," *IEEE Trans. Commun.*, vol. 66, no. 9, pp. 3879-3891, Sept. 2018.
 - [23] H. Li, M. Li and Q. Liu, "Hybrid beamforming with dynamic subarrays and low-resolution PSs for mmWave MU-MISO systems," *IEEE Trans. Commun.*, vol. 68, no. 1, pp. 602-614, Jan. 2020.
 - [24] H. Li, M. Li, Q. Liu and A. L. Swindlehurst, "Dynamic hybrid beamforming with low-resolution PSs for wideband mmWave MIMO-OFDM systems," *IEEE J. Sel. Areas Commun.*, vol. 38, no. 9, pp. 2168-2181, Sept. 2020.
 - [25] K. Ardah, G. Fodor, Y. C. B. Silva, W. C. Freitas and A. L. F. de Almeida, "Hybrid analog-digital beamforming design for SE and EE maximization in massive MIMO networks," *IEEE Trans. on Veh. Tech.*, vol. 69, no. 1, pp. 377-389, Jan. 2020.
 - [26] J. Jiang, Y. Yuan and L. Zhen, "Multi-user hybrid precoding for dynamic subarrays in mmWave massive MIMO systems," *IEEE Access*, vol. 7, pp. 101718-101728, Jul. 2019.
 - [27] R. Magueta, D. Castanheira, A. Silva, R. Dinis, and A. Gameiro, "Hybrid multi-user equalizer for massive MIMO millimeter-wave dynamic subconnected architecture," *IEEE Access*, vol. 7, pp. 79017-79029, Jun. 2019.
 - [28] M. Bayraktar and G. M. Guvensen, "An efficient interference-aware constrained massive MIMO beamforming for mm-Wave JSMD," *IEEE Access*, vol. 9, pp. 87877-87897, Jun. 2021.
 - [29] S. X. Ta, I. Park and R. W. Ziolkowski, "Crossed dipole antennas: A review," *IEEE Antennas Propag. Mag.*, vol. 57, no. 5, pp. 107-122, Oct. 2015.
 - [30] H. Tang, X. Zong and Z. Nie, "Novel broadband dual-polarized antenna for 5G applications," *2018 International Symposium on Antennas and Propagation (ISAP)*, Busan, Korea (South), 23-26 Oct. 2018, pp. 1-2.
 - [31] K. Honda, T. Fukushima and K. Ogawa, "Full-azimuth beam steering MIMO antenna arranged in a daisy chain array structure," *Micromachines*, vol. 11, no. 9, Sep. 2020.
 - [32] V. R. Rentapalli and Z. J. Khan, "MIMO and smart antenna technologies for 3G and 4G," *Information Technology and Mobile Communication*, vol. 147, Springer, Berlin, DOI: 10.1007/978-3-642-20573-6_90.
 - [33] C. Balanis, *Antenna Theory: Analysis and Design*, Wiley, 2016.
 - [34] K. Mahmoud, M. El-Adawy, S. Ibrahim, R. Bansal and S. Zainud-Deen, "A comparison between circular and hexagonal array geometries for smart antenna systems using particle swarm optimization algorithm," *Progress In Electromagnetics Research*, vol. 72, pp. 75-90, 2007.
 - [35] C. Beckman and B. Lindmark, "The evolution of base station antennas for mobile communications," *International Conference on Electromagnetics in Advanced Applications*, Turin, Italy, 17-21 Sept. 2007, pp. 85-92, DOI: 10.1109/ICEAA.2007.4387244.
 - [36] R. F. Harrington, *Field Computation by Moment Methods*, Wiley-IEEE Press, 1993.
 - [37] X. Chen, S. Zhang and Q. Li, "A review of mutual coupling in MIMO Systems," *IEEE Access*, vol. 6, pp. 24706-24719, Apr. 2018.
 - [38] K. Mahmoud, M. El-Adawy, S. Ibrahim, R. Bansal and S. Zainud-Deen, "A comparison between circular and hexagonal array geometries for smart antenna systems using particle swarm optimization algorithm," *Progress In Electromagnetics Research*, vol. 72, pp. 75-90, 2007.
 - [39] J. Wang, L. Zhaobiao, X. Li, "Analysis of MIMO diversity improvement using circular polarized antenna", *Int. J. Antennas Propag.*, vol. 2014, Article ID 570923, doi.org/10.1155/2014/570923.
 - [40] U. Ullah, I. B. Mabrouk and S. Koziel, "Enhanced-performance circularly polarized MIMO antenna with polarization/pattern diversity," *IEEE Access*, vol. 8, pp. 11887-11895, Jan. 2020.
 - [41] 3GPP TS 138 211 Version 15.3.0 Rel.15, 5G NR Physical channels and modulation, 2018.
 - [42] 3GPP TR 38.901 Version 14.3.0 Rel. 14, Study on channel model for frequencies from 0.5 to 100 GHz, 2018.
 - [43] R. Giuliano, C. Monti and P. Loreti, "WiMAX fractional frequency reuse for rural environments," *IEEE Wireless Communications*, vol.15, no. 3, pp. 60-65, Jun. 2008.
 - [44] P. K. Gkonis, P.K.; Trakadas and D. I. Kaklamani, "A comprehensive study on simulation techniques for 5G networks: State of the art, analysis and future challenges," *Electronics*, vol. 9, no. 3, DOI: 10.3390/electronics9030468.